# nature electronics

**Article** 

https://doi.org/10.1038/s41928-024-01127-x

# Monolithically integrated high-density vertical organic electrochemical transistor arrays and complementary circuits

Received: 24 May 2023

Accepted: 18 January 2024

Published online: 21 February 2024



Check for updates

Jaehyun Kim<sup>1,2</sup>, Robert M. Pankow 1, Yongjoon Cho<sup>1</sup>, Isaiah D. Duplessis 1, Fei Qin<sup>1</sup>, Dilara Meli **1** Rachel Daso<sup>4</sup>, Ding Zheng<sup>1</sup>, Wei Huang **1**, Jonathan Rivnay <sup>© 3,4</sup> ⋈, Tobin J. Marks <sup>© 1,3</sup> ⋈ & Antonio Facchetti <sup>© 1,5,6</sup> ⋈

Organic electrochemical transistors (OECTs) can be used to create biosensors, wearable devices and neuromorphic systems. However, restrictions in the micro- and nanopatterning of organic semiconductors, as well as topological irregularities, often limit their use in monolithically integrated circuits. Here we show that the micropatterning of organic semiconductors by electron-beam exposure can be used to create high-density (up to around 7.2 million OECTs per cm<sup>2</sup>) and mechanically flexible vertical OECT arrays and circuits. The energetic electrons convert the semiconductor exposed area to an electronic insulator while retaining ionic conductivity and topological continuity with the redox-active unexposed areas essential for monolithic integration. The resulting p- and n-type vertical OECT active-matrix arrays exhibit transconductances of 0.08–1.7 S, transient times of less than 100 µs and stable switching properties of more than 100,000 cycles. We also fabricate vertically stacked complementary logic circuits, including NOT, NAND and NOR gates.

Organic electrochemical transistors (OECTs) and other organic semiconductor-based electronic components have the potential to be of use in the development of wearable electronics<sup>1-3</sup>, biosensors<sup>4-7</sup> and neuromorphic devices<sup>8-10</sup>, due to properties such as low driving voltages, excellent amplification and sensing capabilities, structural versatility and potential for high-throughput production<sup>11-13</sup>. Recently, the development of conventional OECTs (cOECTs), which have a coplanar source-drain electrode architecture, has led to improved transconductance  $(g_m)$  and switching speed metrics. However, with a few notable exceptions 9,14,15, cOECTs have limited temporal and/or operational stability, slow redox processes and poorly balanced p-(hole-transporting)/n-(electron-transporting) OECT performance. This restricts implementation in advanced signal processing for bioelectronics and multiplexed state-of-the-art electronics<sup>16-18</sup>. Moreover, this architecture severely limits geometric fill-factors for high-resolution and compact complementary circuits. To address these issues, vertically stacked OECT architectures (vertical OECT, vOECT) have been developed<sup>8,19-21</sup>. However, creating scalable patterning methods for the semiconductor materials and optimizing the architectural topology for efficient monolithic integration, is technologically challenging for vOECTs. Such capabilities will though be required to achieve complex, high-density OECT arrays/circuits for multifunctional data analysis<sup>22-25</sup>.

While epitaxial silicon-based and inorganic semiconductors have used photolithography to shrink transistor channel length and pattern all circuit materials, this approach is problematic for organic

Department of Chemistry and Materials Research Center, Northwestern University, Evanston, IL, USA. 2Department of Semiconductor Science, Dongguk University, Seoul, Republic of Korea. 3Department of Materials Science and Engineering, Northwestern University, Evanston, IL, USA. 4Department of Biomedical Engineering, Northwestern University, Evanston, IL, USA. 5Laboratory of Organic Electronics, Department of Science and Technology, Linköping University, SE-60174, Norrköping, Sweden. 6School of Materials Science and Engineering, Georgia Institute of Technology, Atlanta, GA, USA. e-mail: jrivnay@northwestern.edu; t-marks@northwestern.edu; afacchetti6@gatech.edu

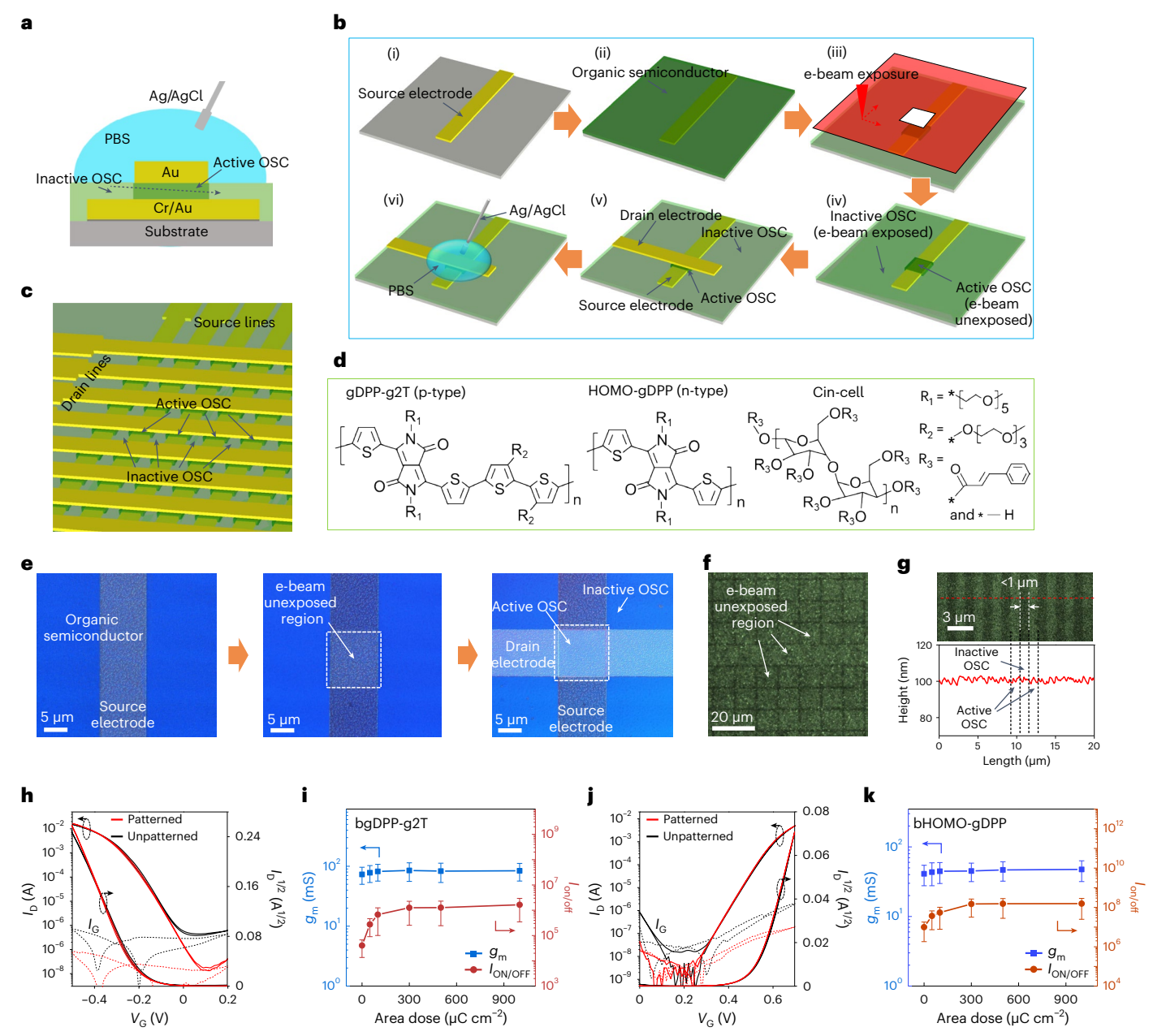


**Fig. 1**| **Fabrication and monolithic integration of vOECTs using e-beam patterning. a**, Cross-sectional illustration of the vOECT architecture used in this study demonstrating the topologically continuous OSC film through the in-channel active and out-of-channel inactive regions. **b**, vOECT fabrication process: (i) thermal evaporation/photolithographic patterning of the bottom source electrode; (ii) spin-coating of the organic semiconductor (OSC); (iii) direct e-beam OSC patterning; (iv) active (e-beam unexposed) and inactive (e-beam exposed) OSCs; (v) thermal evaporation/patterning of the top drain electrode; (vi) application of a phosphate buffer solution (PBS) as the electrolyte and an Ag/AgCl gate electrode. **c**, Illustration of a vOECT array. **d**, Chemical structures of the p-/n-type OSC polymers, gDPP-g2T and HOMO-gDPP, respectively, and the

crosslinkable polymer Cin-Cell. Note, the OSC film is composed by a 9:2 weight blend of bgDPP-g2T or bHOMO-gDPP and Cin-Cell to enhance the functional stability of the device as described in ref. 21. **e**, CPOM images of a bgDPP-g2T vOECT through different fabrication stages ( $W = d = 10 \, \mu m$ ). **f**, CPOM image of a bgDPP-g2T film after direct e-beam exposure. **g**, CPOM image (top) and surface height profile along the cutline (bottom) of a bgDPP-g2T film. **h-k**, Transfer characteristics of bgDPP-g2T (**h**) and bHOMO-gDPP (**j**) vOECTs before and after OSC patterning with a dose of 300  $\mu$ C cm<sup>-2</sup>.  $I_0$  is the drain current. Dependence of the  $g_m$  and  $I_{on/off}$  on the e-beam dose for bgDPP-g2T (**i**) and bHOMO-gDPP (**k**) vOECTs (error bars represent standard deviation for n = 20, mean  $\pm$  s.d.).

semiconductors due to their limited chemical orthogonality with photoresists and typical contamination of the channel material<sup>26,27</sup>. In addition, conventional photolithography with such semiconductors does not address the topological irregularities that prevent vOECT integration into active-matrix circuits. Thus, alternative micro- and nanofabrication strategies for patterning organic semiconductors for vOECTs will be required for integration as well as to suppress parasitic/off-currents, reduce crosstalk between neighbouring

devices and minimize power consumption in high-resolution OECT circuit arrays.

In this Article, we report monolithically integrated high-density p- and n-type vOECT active-matrix arrays and complementary logic circuits. The devices are fabricated using direct electron-beam exposure of both p-and n-channel organic semiconductor (OSC) films. While it is known that e-beam lithography (eBL) can pattern many types of organic and inorganic materials via different types of negative and positive

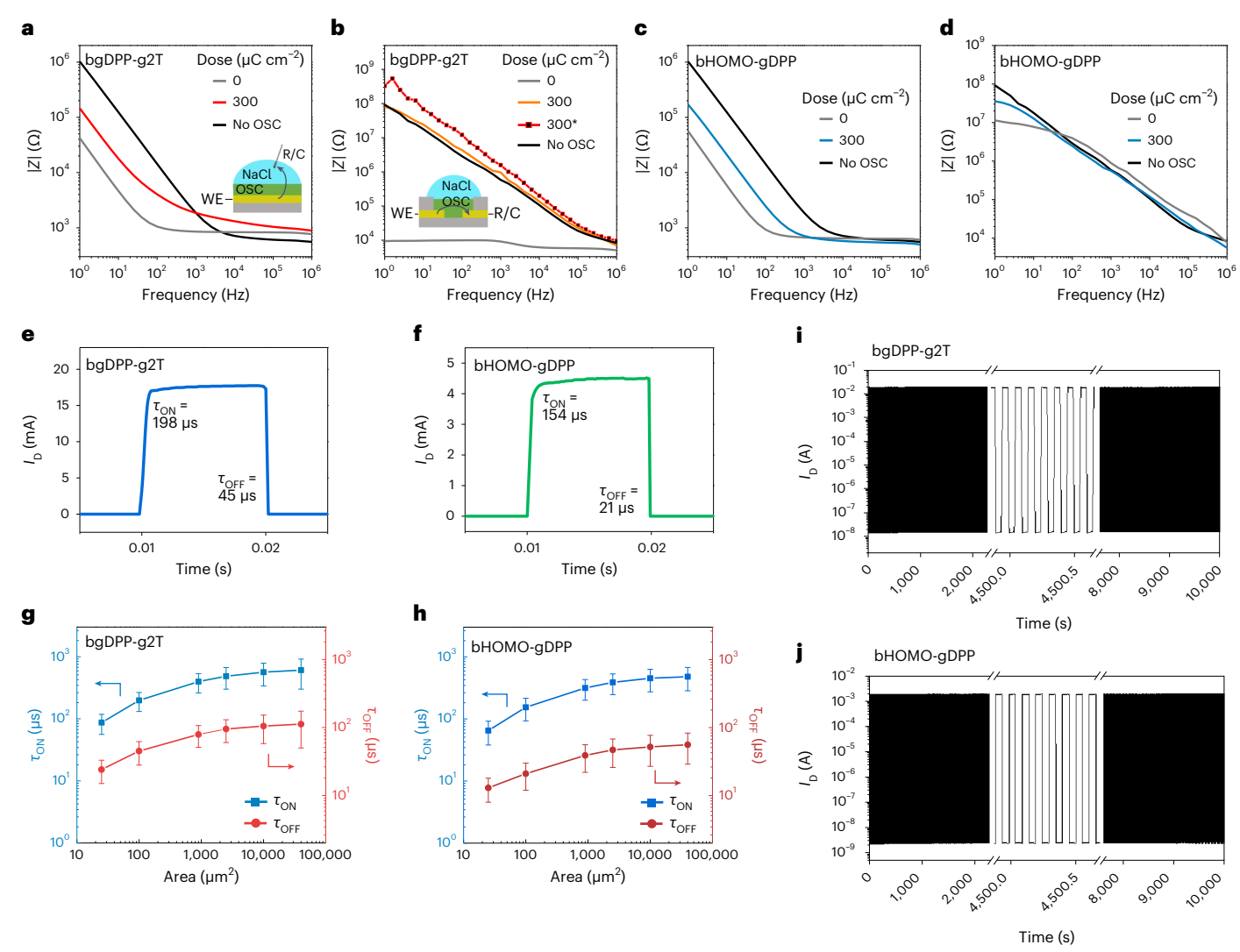


**Fig. 2** | **vOECT ionic and electronic transport characterization and transient response stability. a,c**, Vertical impedance (*Z*) spectra of p- (**a**) and n-type (**c**) OSCs at d.c. bias of 0.5 V and -0.7 V respectively. **b,d**, Lateral impedance spectra of p- (**b**) and n-type (**d**) OSCs at 0.0 V d.c. bias. The insets in **a** and **b** are the vertical and conventional (lateral) EIS testing configurations, respectively. In **b**, 300\* represents data collected when excess electrolyte was removed from the OSC. All data were collected in 0.1 M NaCl (aqueous) with a 0.02 V a.c. oscillation amplitude. **e,f**, Transient response of bgDPP-g2T (**e**) and bHOMO-gDPP (**f**)

vOECTs. For the p-type bgDPP·g2T vOECTs,  $V_G$  is switching between 0 V and -0.5 V with  $V_D = -0.5$  V, and for the n-type bHOMO·gDPP vOECTs,  $V_G$  is switching between 0 V and +0.7 V with  $V_D = +0.5$  V.  $\mathbf{g}$ ,  $\mathbf{h}$ , Dependence of transient time on channel dimensions for bgDPP-g2T ( $\mathbf{g}$ ) and bHOMO·gDPP ( $\mathbf{h}$ ) vOECTs (error bars represent standard deviation for n = 20, mean  $\pm$  s.d.).  $\mathbf{i}$ ,  $\mathbf{j}$ , Cycling stability (frequency of 10 Hz) of bgDPP-g2T ( $\mathbf{i}$ ) and bHOMO-gDPP ( $\mathbf{j}$ ) vOECTs. In all devices  $W = d = 10 \ \mu m$ ,  $L \approx 100 \ nm$ , dose =  $300 \ \mu C \ cm^{-2}$ .

resist chemistries<sup>28,29</sup>, our eBL patterning-based approach offers three additional advantages. First, semiconductor patterning is achieved without using masks, resists, developing solvents or stripping; instead, the OSC out-of-channel region is directly exposed to the e-beam, making it electronically inactive (insulating) but still ionically conductive. This eliminates the need for chemical solvents that can damage the OSC and produce additional chemical waste. Second, ultra-small and high-density vOECTs can be fabricated with well-defined and patterned electronically active (conducting) channel regions due to the high-resolution of e-beam exposure (down to the submicrometre scale). Third, multilayer integration of high-performance and high-density OECT structures is now possible due to the presence of a planarized OSC films, which are topologically smooth and continuous. With the approach, we fabricate monolithically integrated OECT arrays with transconductances ranging from 0.08-1.7 S, transient times below 100 μs, densities up to ~7.2 million OECT cm<sup>-2</sup> and stabilities of greater than 100,000 cycles.

# **Semiconductor film patterning**

The schematic representations and fabrication of a single vOECT and a monolithically integrated vOECT array are shown in Fig. 1a-c (see Methods for details). As OSC channel materials, we employ recently developed blends consisting of a redox-active polymer, gDPP-g2T for the p-type OECTs and HOMO-gDPP for the n-type OECTs, with a redox-inert photo-crosslinkable cinnamate-cellulose polymer (Cin-Cell) in an optimal weight ratio of 9:2 (ref. 21) (Fig. 1d). Note, unless specifically indicated, all experiments were carried out using blends of OSC + Cin-Cell, which we refer to hereafter as bgDPP-g2T and bHOMO-gDPP. The OSC films were deposited by spin-coating the corresponding blend solution onto an Au source electrode (or Au parallel line electrodes for arrays) which is (are) patterned by conventional photolithography (see cross-sectional scanning electron microscopy (SEM) images in Supplementary Fig. 1). Next, the area outside the channel region(s) is e-beam irradiated (up to 1,000 μC cm<sup>-2</sup>), which is an energy exceeding those of typical C-C (3.63 eV), C-H (4.25 eV),

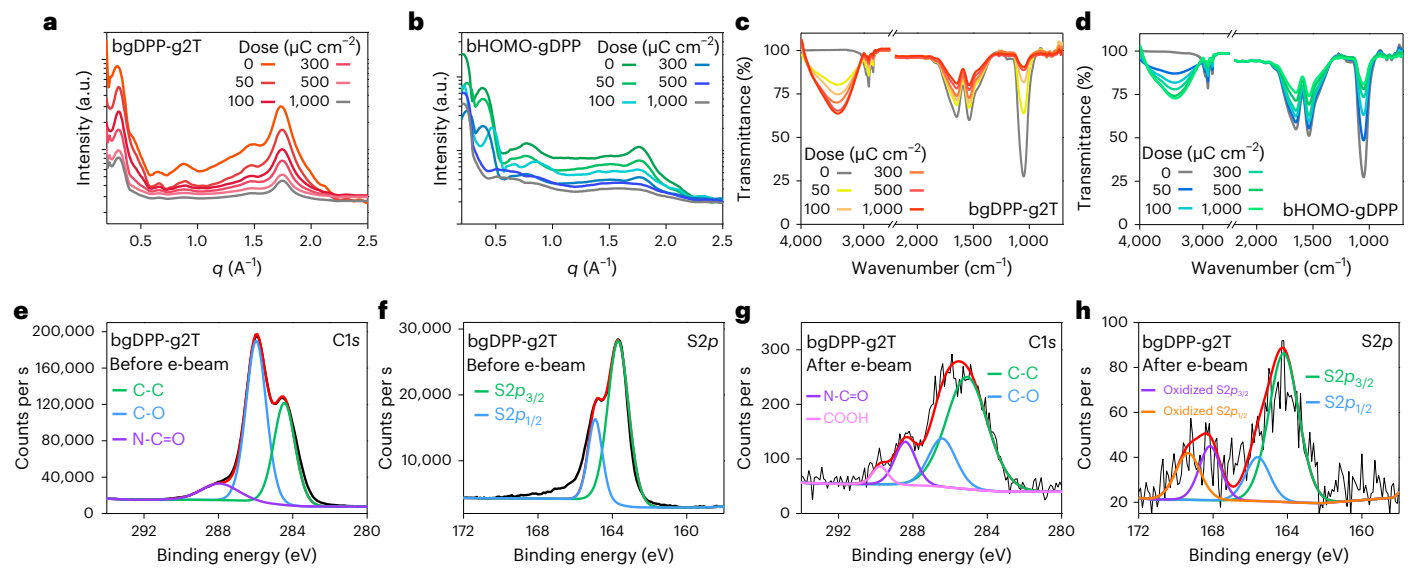


**Fig. 3** | **Characterization of e-beam unexposed and exposed OSC films. a,b**, Out-of-plane one-dimensional line-cuts for GIWAXS patterns of bgDPP-g2T (**a**) and bHOMO-gDPP (**b**) films under different e-beam doses. *q* is the wave vector. **c,d**, FTIR spectra of bgDPP-g2T (**c**) and bHOMO-gDPP (**d**) films under

different e-beam doses. **e**–**h**, Deconvoluted XPS spectra of bgDPP-g2T films in the spectral regions of C1s (**e**,**g**) and S2p (**f**,**h**) before (**e**,**f**) and after (**g**,**h**) e-beam exposure (dose = 300  $\mu$ C cm<sup>-2</sup>).

C=C (6.34 eV) and C=O (7.59 eV) bonds<sup>30</sup>. Thus, e-beam exposure can disrupt charge transport in the exposed region by a combination of several mechanisms including chemical bond scission, new bond formation and disruption of crystalline order<sup>31</sup>. A second perpendicularly arranged Au drain electrode (Au lines) is (were) thermally evaporated and patterned by photolithography, yielding devices with a channel length (L) corresponding to the OSC film thickness (~100 nm) and a channel area ( $W \times d$ , see Fig. 1e) given by the overlap between the two Au lines (in most experiments, 10 μm × 10 μm). Figure 1e, f shows the cross-polarized optical microscopy (CPOM) images during/after vOECT fabrication which indicate that upon e-beam irradiation, the semiconductor film loses typical strong birefringence characteristic of the ordered semicrystalline morphology. Note, the e-beam exposure also allows submicrometre patterning of both bgDPP-g2T and bHOMO-gDPP as shown in the CPOM images of Fig. 1g (top) and Supplementary Fig. 2, respectively. The device (array) is completed by dispensing a PBS electrolyte solution and using an Ag/AgCl gate electrode. Note, achieving patterned electronically active islands surrounded by electronically inactive areas, which are continuous and non-relief as shown in the linecut of Fig. 1g (bottom) is key to the present system-level circuit integration.

Representative transfer characteristics and electrical performances of unpatterned/e-beam patterned bgDPP-g2T and bHOMO-gDPP vOECTs at different e-beam doses are shown in Fig. 1h-k and Supplementary Fig. 3 with all performance parameters collected in Supplementary Table 1. These data demonstrate excellent switching behaviour for both p- and n-type patterned devices, achieving maximum drain currents  $(I_{ON})$  of  $1.7 \times 10^{-2}$  A (drain voltage  $(V_D) = -0.5$  V, gate voltage  $(V_G) = -0.5 \text{ V}$ ) and  $4.3 \times 10^{-3} \text{ A}$   $(V_D = +0.5 \text{ V}, V_G = +0.7 \text{ V})$ , respectively, with transconductances ( $g_m$ ) of 82.9 mS and 45.1 mS, respectively. Note, the performance parameters stabilize at a dose of ~300 μC cm<sup>-2</sup>, while without patterning of the semiconducting layer comparable  $g_m$  values are achieved (72.7 mS and 41.1 mS, respectively), but the on/off current ratios ( $I_{ON/OFF}$ ) are remarkably lower (4.1 × 10<sup>4</sup> and  $9.9 \times 10^6$  (unpatterned) versus  $1.3 \times 10^6$  and  $1.5 \times 10^8$  (patterned), respectively). In addition, the gate leakage currents for both p- and n-type vOECTs are decreased after patterning of the OSC layer (~10<sup>-6</sup> A (unpatterned) versus 10<sup>-7</sup> A (patterned)). Thus, this channel patterning procedure substantially decreases both the off current  $(I_{OFF})$  and

the gate current ( $I_{\rm G}$ ), which are known to increase circuit static power consumption, and simultaneously suppresses crosstalk in the present OECT arrays. In addition, area-normalized  $g_{\rm m}(g_{\rm m,A})$  and  $I_{\rm ON}(I_{\rm ON,A})$  values for p- and n-type vOECTs, given by  $g_{\rm m,A}=g_{\rm m}/(Wd)$  and  $I_{\rm ON,A}=I_{\rm ON}/(Wd)$  (ref. 31), are 829  $\mu$ S  $\mu$ m<sup>-2</sup> (16.7 kA cm<sup>-2</sup>) and 451  $\mu$ S  $\mu$ m<sup>-2</sup> (4.3 kA cm<sup>-2</sup>), respectively. As a control, vOECTs were also fabricated by e-beam irradiation of the entire semiconductor film, including the channel, and were found to be essentially inactive (Supplementary Fig. 4). Thus, in the present vOECT architecture the semiconductor channel area is only 'electronically patterned' while remaining physically connected to the e-beam exposed, and electronically inactive, out-of-channel region.

#### Ionic and electronic charge transport

An important question here is whether the e-beam exposed vOECT area remains ionically conductive since this would also allow ions to enter the device channel over the entire perimeter defined by the crossed electrodes, versus only two segments as in our previously reported vOECT architecture (see cartoon in Supplementary Fig. 5)<sup>32-35</sup>. To validate the ionic transport efficiency in the OSC, electrochemical impedance spectroscopy (EIS) measurements were carried out for both p- and n-type semiconductor films as a function of e-beam exposure time. EIS experiments were conducted in vertical and lateral configurations (Supplementary Fig. 6)<sup>36</sup>. Impedance-frequency spectra of both bgDPP-g2T and bHOMO-gDPP show a clear increase in impedance at 0.5 V and -0.7 V, respectively, confirming that electronic charge coupling is reduced by e-beam exposure (Fig. 2a,c). For bgDPP-g2T, this change in material behaviour is seen more obviously in the lateral EIS, where the shape of the impedance spectrum changes entirely, as seen in the large increase in impedance (Fig. 2b). Fitting this curve to an equivalent circuit, it can be seen that the electronic impedance across the film increases 100,000-fold after e-beam exposure (Supplementary Table 2). Fits of the ionic resistance, however, show that it remains relatively unchanged at  $4.1 \text{ k}\Omega$  and  $4.4 \text{ k}\Omega$  for neat and exposed samples, respectively. Due to the higher threshold voltage of the n-type, the device is 'off' at 0 V before and after e-beam exposure. As such, it is not unexpected to see smaller differences in the spectra measured on the lateral devices, where both show limited electronic conductivity and similar ionic conductivity (Fig. 2d and Supplementary Table 2). Thus, we confirm that e-beam irradiation

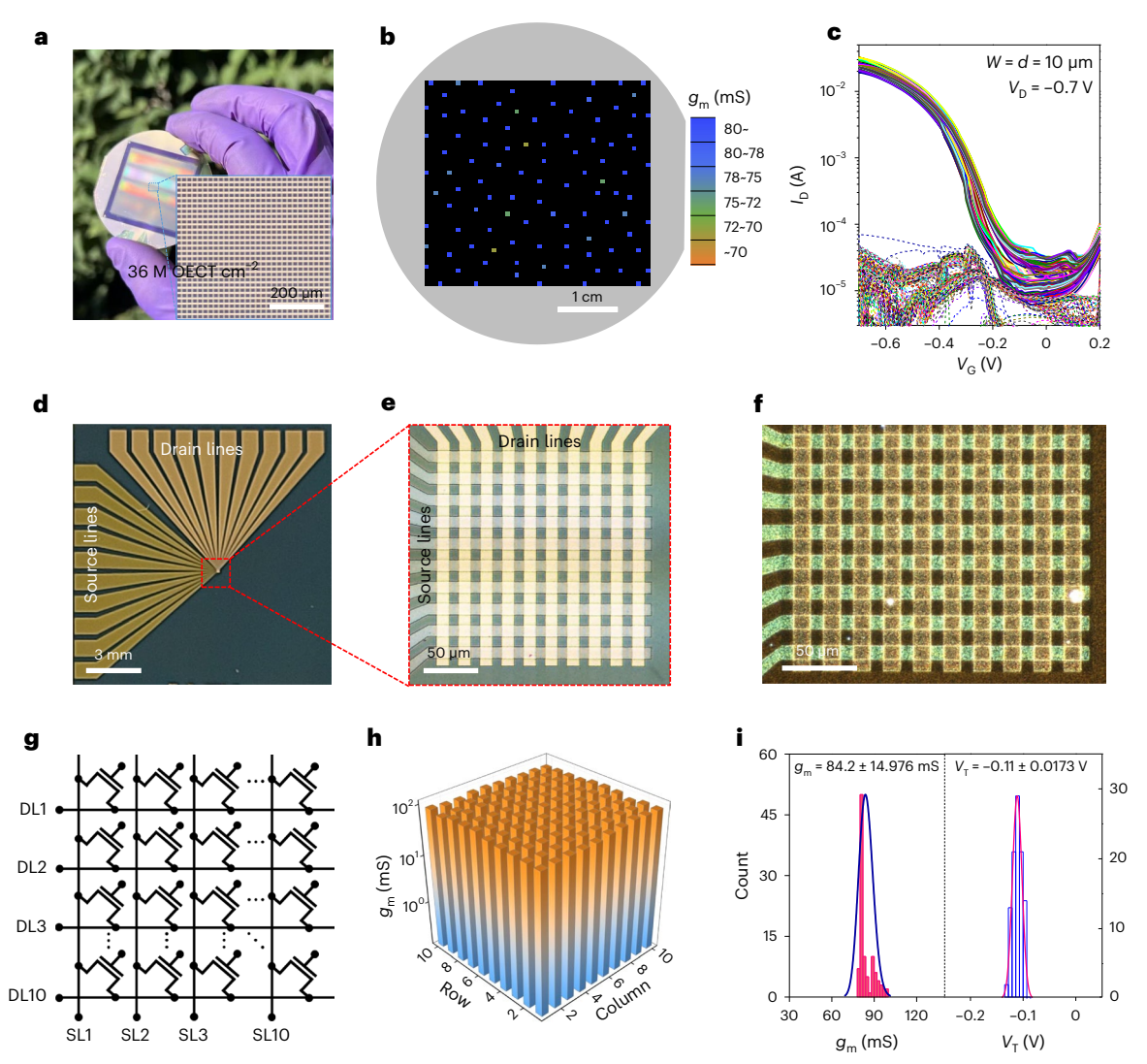


**Fig. 4** | **High-density monolithically integrated vOECT arrays fabricated by e-beam exposure. a**, Photograph of 2-inch wafer-scale vOECT arrays comprising bgDPP-g2T OECTs. Inset, zoomed-in microscope image of the vOECT arrays. **b**, Transconductance map of the wafer-scale vOECTs; the spots indicate the measured devices. **c**, Transfer characteristics of 100 bgDPP-g2T vOECTs ( $W = d = 10 \, \mu \text{m}$ ). **d**-**f**, Low (**d**) and high (**e**) magnification optical microscopy

images, and CPOM image ( $\mathbf{f}$ ) of a bgDPP-g2T vOECT array.  $\mathbf{g}$ , Circuit schematic of  $10 \times 10$  vOECT active-matrix arrays (DL = drain line, SL = source line).  $\mathbf{h}$ , Transconductance distribution in the  $10 \times 10$  bgDPP-g2T vOECT arrays.  $\mathbf{i}$ , Statistical distribution histograms of transconductance (left) and threshold voltage (right) for 100 devices, which are all functioning.

maintains the ionic conductivity of both p- and n-type organic semiconductor blends.

In addition, the  $I_{ON}$ ,  $g_m$  and transient response times of the present vOECTs with respect to the semiconductor channel dimension were also analysed (Fig. 2e,f and Supplementary Fig. 7). We find that  $I_{\rm ON}/g_{\rm m}$  of both p-vOECTs and n-type vOECTs increase linearly from  $9.2 \times 10^{-3} \text{ A}/42.7 \text{ mS to } 3.6 \times 10^{-1} \text{ A}/1.7 \text{ S} \text{ and from } 2.3 \times 10^{-3} \text{ A}/24.2 \text{ mS}$ to  $9.1 \times 10^{-2}$  A/0.7 S, respectively, while the turn-on  $(\tau_{ON})$ /turn-off  $(\tau_{\rm OFF})$  transient times decrease from 607/112 µs to 87/24 µs, and from 479/56  $\mu$ s to 65/13  $\mu$ s, respectively, as the  $W \times d$  channel dimension is decreased from  $200 \times 200$  to  $5 \times 5 \mu m^2$  (Fig. 2g,h and Supplementary Fig. 8), a result in accord with faster ion exchange in smaller devices and among the shortest reported values for OECTs and comparable with state-of-the-art electronics<sup>9,21,37-42</sup>. Furthermore, the transient response characteristics were also measured to demonstrate the stability of both the p- and n-type vOECTs. As shown in Fig. 2i, j, the present vOECTs sustain more than 100,000 repeated switching cycles with negligible performance degradation, thus being among the most stable OECT devices reported to date<sup>43,44</sup>.

# Semiconductor film characterization

Before attempting monolithic integration, the effects of OSC e-beam exposure were investigated by multiple techniques to understand the origin of the semiconductor electronic patterning. Two-dimensional grazing incidence wide-angle X-ray scattering (2D-GIWAXS) patterns of the pristine/unexposed bgDPP-g2T and bHOMO-gDPP films exhibit strong out-of-plane and in-plane reflections typical of these semicrystalline polymers (Supplementary Fig. 9)21. Upon e-beam exposure the intensity of all reflections falls as the e-beam dose increases from 50 to 1,000 μC cm<sup>-2</sup>, as shown in the GIWAXS one-dimensional line-cuts of both polymers (Fig. 3a,b). Amorphization can occur via molecular reorganization and/or chemical decomposition. To address this point, Fourier transform infrared (FTIR) spectroscopy, ultraviolet (UV)-visible-near IR spectroscopy and X-ray photoelectron spectroscopy (XPS) measurements were carried out. The FTIR spectra of the semiconductor films show strong absorptions at 2,800-3,000 cm<sup>-1</sup>, 1,500-1,700 cm<sup>-1</sup> and 1,000-1,200 cm<sup>-1</sup> assignable to C-H, C=C/C=O and C-C/C-O stretching modes in these polymers<sup>45</sup> (Fig. 3c,d). The intensity of all peaks decreases upon increasing the e-beam irradiation

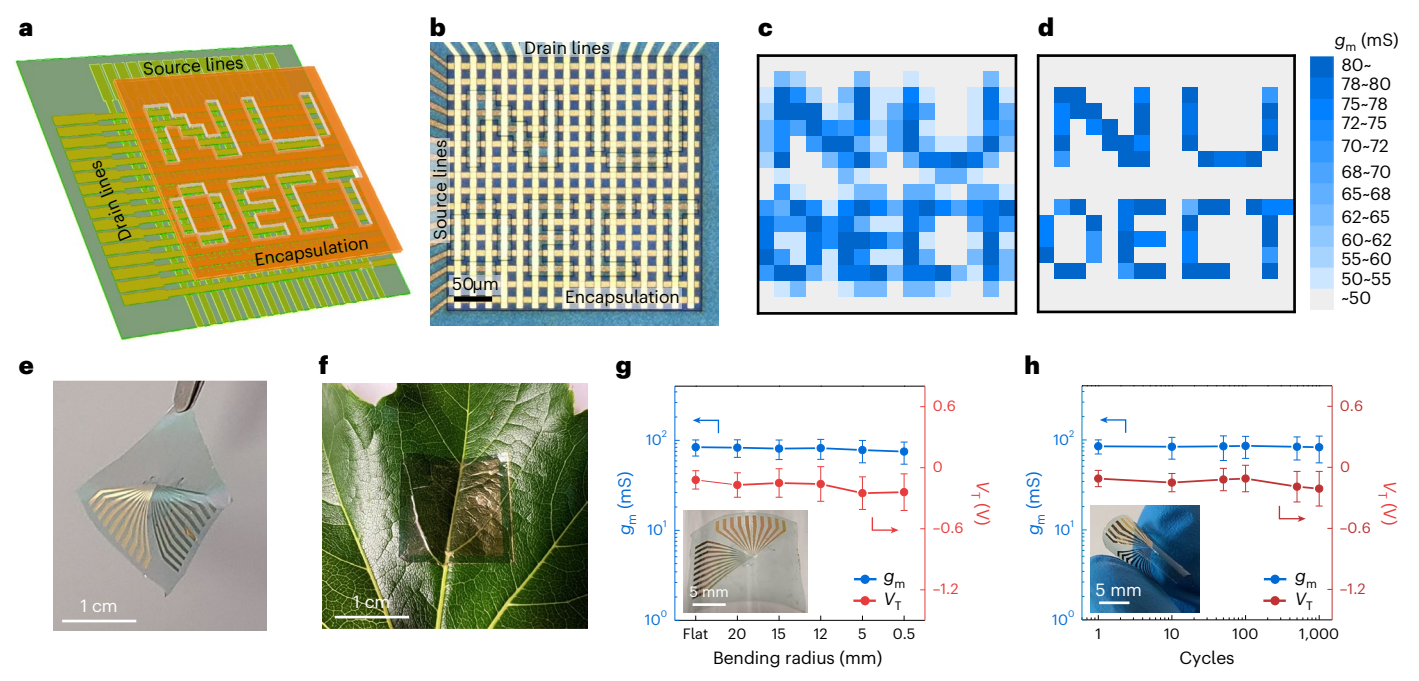


**Fig. 5** | **2D** areal mapping and flexible vOECT arrays. **a**,**b**, Schematic illustration (**a**) and optical microscope image (**b**) of  $16 \times 16$  vOECT active-matrix arrays. **c**,**d**, Transconductance profile of  $16 \times 16$  vOECT arrays before (**c**) and after (**d**) semiconductor channel patterning via e-beam exposure. **e**,**f**, Optical images of a free standing flexible vOECT array delaminated from the glass carrier substrate (**e**) and laminated to a fig leaf (**f**). **g**, Change of transconductance

and threshold voltage during in situ bending tests of a flexible bgDPP-g2T vOECT array as a function of bending radius. **h**, Change of transconductance and threshold voltage of bgDPP-g2T vOECTs under mechanical strain (bent at 0.5 mm radius) during 1,000 cycles. **g**, **h**, Error bars represent standard deviation for n = 20, mean  $\pm$  s.d. Inset, optical image of the flexible vOECTs. In all devices  $W = d = 10 \mu \text{m}$ ,  $L \approx 100 \text{ nm}$  and dose =  $300 \mu \text{C cm}^{-2}$ .

dose while a broad peak appears and intensifies at 2,800-3,000 cm<sup>-1</sup> (Supplementary Table 3). The latter can be assigned to one or more O-H stretching modes. Interestingly, the intensity of the peaks at 1,000-1,200 cm<sup>-1</sup> decreases to a greater extent than those of the others indicating that most of the e-beam promoted reactions occurs at/ near the C-O bonds, and therefore in the DPP portion of the polymer. In addition, UV-visible-near infrared spectra of the polymer films indicate that the strong intramolecular charge transfer absorption bands at 890 nm for bgDPP-g2T and 975 nm for Homg-gDPP decrease in intensity (~85% and ~86%, respectively) and blue-shifts (811 nm and 838 nm, respectively) as the e-beam dose reaches 1.000 uC cm<sup>-2</sup>. suggesting that reactive species disrupt the polymer backbone  $\pi$ -conjugation (Supplementary Fig. 10 and Supplementary Table 4). Furthermore, XPS measurements in Fig. 3e-h and Supplementary Fig. 11 reveal the incorporation of oxygen as evidenced by formation of completely new peaks in the C1s, S2p and O1s at binding energies of 289.76 eV (C(=O)-OH), 168.16 and 169.34 eV (S-O) and 535.70 eV (C(=O)-OH), respectively (Supplementary Table 5). Finally, film morphology accessed by atomic force microscopy (AFM) (Supplementary Fig. 12) indicates phase separation between the p-/n-polymer and the Cin-Cell additive in both pristine/e-beam exposed blends, as reported for the e-beam unexposed films in our previous work<sup>21</sup>. Interestingly, the root-mean-square roughnesses of these films decrease from 3.1 to 2.6 nm (bgDPP-g2T) and 3.7 to 3.2 nm (bHOMO-gDPP) upon exposure, in accord with reduced texturing of the e-beam exposed films (Supplementary Table 6). Overall, the chemical and physical analyses support the model in which semiconductor film electronic patterning and amorphization, mainly occur via backbone deconjugation upon uptake of oxygen as hydroxylated species and not backbone/ chain fragmentation.

# High-resolution vOECT active-matrix arrays

Next, vOECT active-matrix arrays of varying dimensions ( $W = d = 10 \mu m$ , metal line separation = 10  $\mu m$ ) were fabricated to demonstrate

monolithic integration with an OECT density of 3.6 M cm<sup>-2</sup> and to analyse response statistics at both the macro- and micro-scale (see optical microscope images in Fig. 4a). First, for a bgDPP-g2T (p-type) 1,440 × 1,440 vOECT array fabricated on a 2-inch wafer (>2 M vOECTs), the transfer characteristics of 100 devices across the entire area were measured to assess reliability (Fig. 4b,c) and exhibit outstanding device uniformity with an average  $g_m$  of 85.7  $\pm$  14.8 mS and a threshold voltage  $(V_T)$  of  $-0.11 \pm 0.03$  V (Supplementary Fig. 13). Next, various batches of 10 × 10 p- and n-type vOECT arrays were fabricated (see optical microscope/CPOM images and equivalent circuits in Fig. 4d-g). All p-/n-type vOECT arrays exhibit highly uniform performance with an average  $g_{\rm m}$  of 84.2 ± 14.9 and 43.1 ± 9.1 mS and  $V_{\rm T}$  of -0.11 ± 0.02 and 0.44 ± 0.015 V, respectively (Fig. 4h,i and Supplementary Fig. 14). Note that all vOECT and complementary inverter pixels in arrays are controlled by a common gate. While this integration is not suitable for active-matrix applications it is important for numerous biomedical applications requiring a grounded reference electrode in cell cultures and tissues where the gate contact can be a large electrode located away from the active recording area. In these cases, variation of single OECT pixel conductance is the result of local variation in ionic strength, ion type and effective gate bias at the device due to the intimate contact of the OECT array with the organ/tissue of interest.

Also fabricated were  $16 \times 16$  bgDPP-g2T vOECT active-matrix arrays, patterned by parylene encapsulation so as to display 'NU OECT' capital letters at the centre and assess the effects of OSC patterning on pixel crosstalk (Fig. 5a,b and detail in Methods). The 2D areal mapping of the array electrochemical signal  $(g_m)$  was characterized as shown in Fig. 5c (unpatterned) and Fig. 5d (patterned), clearly demonstrating the absence of crosstalk for the patterned vOECT array. Finally, we also fabricated a bgDPP-g2T  $10 \times 10$  vOECT array on a flexible parylene substrate  $(2 \, \mu \text{m}$  thick, Fig. 5e,f) which exhibits excellent performance metrics  $(g_m = 85.4 \pm 15.147 \, \text{mS}, V_T = -0.11 \pm 0.08 \, \text{V})$  as well as outstanding stability  $(g_m$  and  $V_T$  variation < 2% under various bending radii (from  $\infty$  to  $0.5 \, \text{mm}$ ) and mechanical cycling  $(0-1,000 \, \text{times})$ 

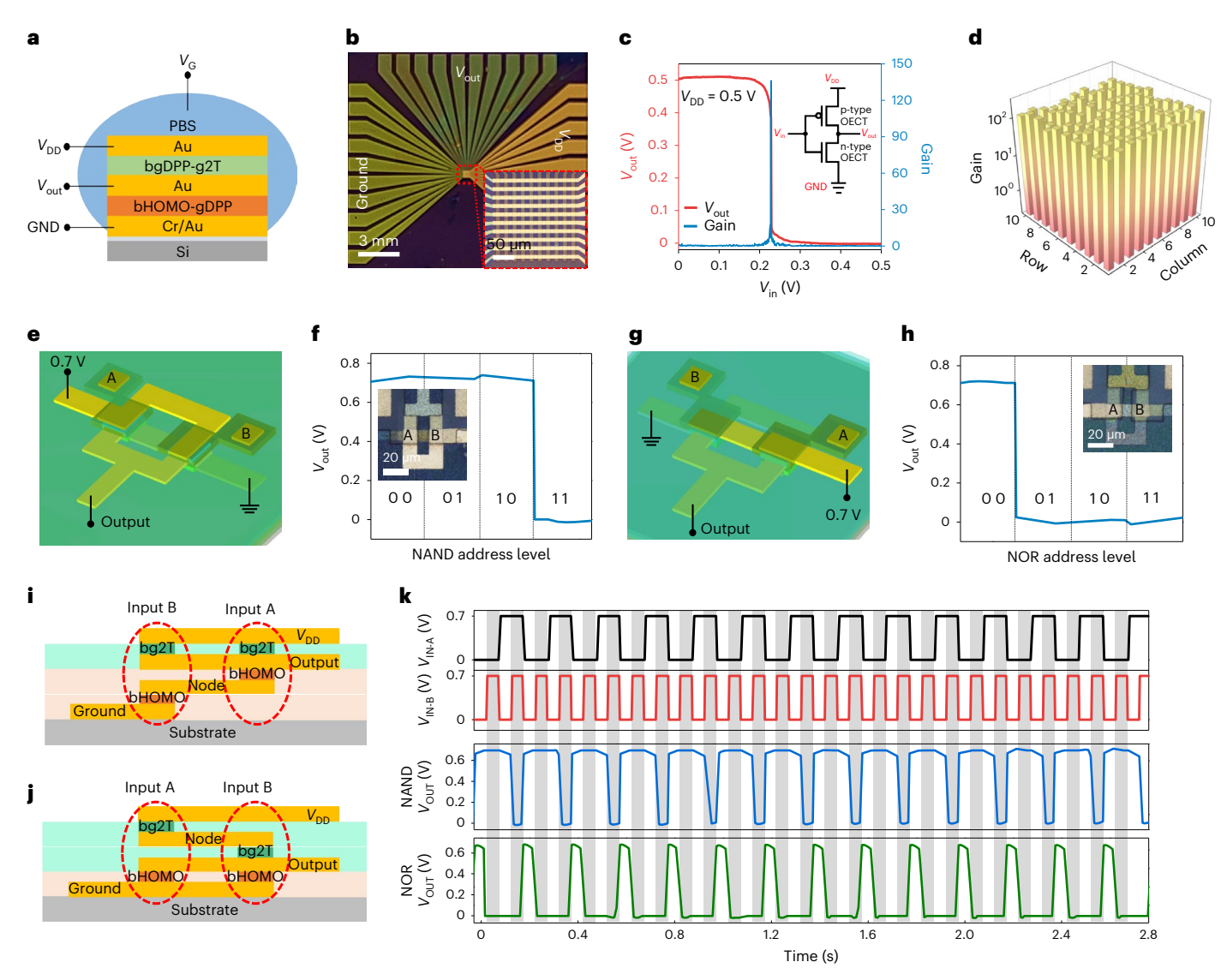


Fig. 6 | High-resolution vertically stacked complementary circuits. **a,b**, Schematic illustration (**a**) and optical microscope image (**b**) of a  $10 \times 10$  VSCI array based on p- and n-vOECTs. **c**, A representative voltage output characteristic of a VSCI along with the voltage gain. **d**, Voltage gain distribution in a  $10 \times 10$  VSCI array. Note, for VSCI arrays measurement, the PBS electrolyte is applied with

the Ag/AgCl gate electrode. **e, f,** Illustration (**e**) and output characteristics (**f**) of a NAND logic circuit. Inset, optical image of the NAND. **g,h**, Illustration (**g**) and output characteristics (**h**) of a NOR logic circuit. Inset, optical image of the NOR. **i,j**, Cross-sectional illustration of NAND (**i**) and NOR (**j**). **k**, Switching stability of VSCI logic circuits. In all devices  $W = d = 10 \mu \text{m}$  and  $L \approx 100 \text{ nm}$ .

deformations (Fig. 5g,h). Note, while the current begins to degrade over longer times because of electrolyte solvent evaporation, the performance recovers by rinsing the devices with water and using a fresh electrolyte drop (Supplementary Fig. 15). These observations indicate that the present vOECT platforms are intrinsically stable.

# Vertically stacked complementary logic circuits

Next, high-resolution vertically stacked complementary inverter (VSCI) arrays, where p-type vOECTs are stacked on top of n-type vOECTs, were fabricated for integrated circuits. The VSCI cross-section and an optical microscope image of a  $10\times10$  VSCI array are shown in Fig. 6a,b, respectively. Note that the present non-relief organic semiconductor patterning method using e-beam exposure can achieve a density of ~7.2 M OECTs cm $^{-2}$ , which is >700–70,000 times more than in previous seminal studies  $^{23,46}$  and OECT arrays  $^{47,48}$ . Note that this circuit would be impossible to fabricate using our previous vOECT fabrication approach  $^{20}$ , where the OSC is patterned/etched, since the top and bottom electrode lines would otherwise make an electrical contact, leading to a short circuit (see cartoon in Supplementary Fig. 16).

A representative output characteristic of a VSCI is reported in Fig. 6c, which varies from 0.5 V to GND (ground, 0 V) by changing the input voltage from 0 to 0.5 V. This array exhibits an average voltage gain of 135.68 ± 30.72 (Fig. 6d). The excellent performance and uniformity of these VSCI structures encouraged the realization of large-scale and high-resolution complementary circuits. Thus, two-input NAND and NOR logic gates consisting of two p- and two n-type vOECTs with a side-gate architecture and a solid-state ion-gel gate dielectric (for ion-gel preparation, see Methods) were demonstrated (Fig. 6e-j and Supplementary Fig. 17)<sup>49,50</sup>. A poly(3,4-ethylene-dioxythiophene):po lystyrene sulfonate PEDOT:PSS) layer/Au side-gate was employed to decrease the electrochemical impedance between the metal gate and the ion-gel dielectric layer (Supplementary Fig. 18)<sup>9,51,52</sup>. Indeed, these vOECT arrays with patterned gates and solid-state electrolytes exhibit outstanding device stability with excellent performance metrics as shown in Supplementary Fig. 19. Using this vertically stacked complementary circuit design the fidelity and spatial resolution of the logic circuits is notably increased. Both circuits exhibit well-defined and highly stable '1' and '0' output logic levels depending on various input

levels (Fig. 6k) and afford a remarkable integration, with a small circuit dimension of only -300  $\mu$ m<sup>2</sup>, which is less than 17,500-fold smaller than in previous reports<sup>21</sup>.

#### Conclusions

We have reported high-performance vOECTs for monolithically integrated complementary logic circuits. The spatially selective e-beam exposure strategy provides direct and high-resolution patterning of organic semiconductors with excellent uniformity, high yield and scalable pattern formation. Moreover, definition of semiconducting-active channel islands that transition into semiconducting-inactive regions enables active-matrix pixilation, which is impossible when using conventional etch-patterned methodologies. Our approach should help broaden the use of OECT circuits in fields such as biological systems, neuromorphic electronics and wearable electronics.

#### **Methods**

#### **Materials synthesis**

The compounds 3,6-bis(5-bromothiophen-2-yl)-2,5-di (2,5,8,11,14-pentaoxahexadecan-16-yl)-2,5-dihydropyrrolo[3,4-c] pyrrole-1,4-dione (1) (ref. 21) 5,5'-bis(trimethyltin)-3,3'-bis (2-(2-(2-methoxyethoxy) ethoxy)ethoxy)-2,2'-bithiophene (2) (ref. 53) and the Cin-Cell<sup>54</sup> polymer were synthesized and purified according to previously reported procedures. Hexabutyldistannane (3) was purchased from Sigma-Aldrich. For the synthesis of polymer bgDPP-g2T, 92.67 mg of compound 1 (0.1 mmol), 81.62 mg of compound 2 (0.1 mmol), 3.00 mg of Pd<sub>2</sub>(dba)<sub>3</sub> and 7.60 mg of P(o-tol)<sub>3</sub> were mixed and pump-purged for three cycles with nitrogen, and then 1.5 ml of anhydrous toluene and 1.5 ml of dimethylformamide were added. The reaction vessel was then sealed and heated at 110°C for 12 h. Then, the polymer was end-capped with 20 μl of 2-(tributylstannyl)-thiophene and 50 µl of 2-bromothiophene and heated at 110°C for 1 h. After cooling, the mixture was mixed with 100 ml of MeOH and 1 ml of concentrated HCl. The precipitate was filtered, dried and purified by Soxhlet extraction using methanol, acetone, hexane and then chloroform. The chloroform portion was concentrated and poured into 100 ml of MeOH. The resulting gDPP-g2T polymer was obtained by vacuum filtration as a black solid (Mn =  $39.7 \text{ kg mol}^{-1}$ , yield 94%). The HOMO-gDPP polymer was synthesized using the same method with 199.00 mg of compound **1** (0.21 mmol) and 124.57 mg of compound **3** (0.21 mmol), 5.00 mg of Pd<sub>2</sub>(dba)<sub>3</sub> and 13.00 mg of P(o-tol)<sub>3</sub> were used as starting materials. The pure HOMO-gDPP polymer was obtained as a black solid  $(Mn = 16.4 \text{ kg mol}^{-1}, \text{ yield } 86\%).$ 

**Vertical OECT and vertical complementary circuit fabrication Solution preparation.** For the semiconductor solution, gDPP-g2T, HOMO-gDPP and Cin-Cell were dissolved in chloroform (20 mg ml<sup>-1</sup> concentration) and the solutions were stirred for >8 h before use. Next these solutions were filtered through a 0.45 µm polyvinylidene difluoride filter and the gDPP-g2T or HOMO-gDPP solution was mixed with the Cin-Cell solution in a volume ratio of 9:2 before use. For the ion-gel solution, 1-ethyl-3-methylimidazolium bis(trifluoromethylsulfonyl) imide (EMIM-TFSI, Sigma-Aldrich) and poly(ethylene glycol)diacrylate (PEGDA, Sigma-Aldrich) were mixed with a volume ratio of 8:2, and 2-hydroxy-2-methyl-propiophenone (HOMPP, Sigma-Aldrich) was added to the mixture with a volume concentration of 3%. The final solution was stirred at 80°C for 6 h.

**Vertical OECT array fabrication.** A Si wafer with a 300 nm thick thermally grown  $SiO_2$  was used as the substrate and it was cleaned by ultrasonication in acetone and next isopropyl alcohol and finally treated with an oxygen plasma for 5 min. For the flexible devices, a 2- $\mu$ m-thick parylene film was used as the substrate, which was deposited on carrier glass by a parylene coater (Specialty coating system, PDS 2010, KISCO Company) via chemical vapour deposition. For the electrical contact,

3 nm of Cr and 150 nm of Au were thermally evaporated as the bottom source electrode and patterned by photolithography. Next, the semiconductor blend solution was spin-coated onto the substrate at 3,000 r.p.m. for 20 s and the resulting film was patterned by e-beam exposure and then cross-linked by UV irradiation (65 mW cm<sup>-2</sup>) for 30 s (Inpro Technologies F300S). A 150 nm Au film was deposited by thermal evaporation as the top drain electrode and patterned by photolithography. For the photolithographic patterning of the source and drain electrodes, the S1813 photoresist was fist spin-coated on the Au film and then exposed to UV light using maskless aligner (MLA 150). Next, the S1813 photoresist film was developed by soaking the substrates in the AZ400K Au etchant solution. Finally, the remaining S1813 photoresist film was stripped with acetone. A phosphate buffer solution (PBS, 1×) was used as the electrolyte and an Ag/AgCl electrode as the gate. When used, the encapsulation layer was prepared by spin-coating SU-8-2002 at 3,000 r.p.m. for 20 s and the resulting film baked at 95°C for 5 m and patterned by photolithography. For the solid-state ion-gel gate dielectric-based devices, a PEDOT:PSS (Clevios PH1000, Heraeus) with 1% of 3-glycidyloxypropyl)trimethoxysilane (GOPS) solution (as a cross-linker) was spin-coated at 2,000 r.p.m. for 20 s on the Au gate electrode and the resulting film (~200 nm thick) patterned by a lift-off process<sup>55</sup>. Finally, the ion-gel solution was drop-cast onto the side-gate device as the gate dielectric and patterned by photolithography<sup>50</sup>.

Complementary vertical inverter array fabrication. The opposite type of semiconductor blend solution was spin-coated onto the first vOECT device/array at 3,000 r.p.m. for 20 s, patterned by e-beam exposure and then cross-linked by UV irradiation as described above. Next, a 150-nm-thick Au electrode functioning as the voltage drain-to-drain ( $V_{\rm DD}$ ) was fabricated as described for the source/drain contacts. PBS (1×) and Ag/AgCl served as the electrolyte and the gate electrode/ $V_{\rm IN}$ , respectively.

Vertical NAND fabrication. A Si/SiO<sub>2</sub> wafer substrate was cleaned as described previously. First, 3 nm of Cr and 150 nm of Au were thermally evaporated as the ground electrode and patterned by photolithography. Next, the n-type bHOMO-gDPP blend solution was spin-coated at 3,000 r.p.m. for 20 s, patterned by e-beam exposure and then cross-linked by UV. A 150 nm Au was deposited by thermal evaporation as the node electrode and patterned by photolithography. Next, the n-type bHOMO-gDPP blend solution was spin-coated again at 3,000 r.p.m. for 20 s, patterned by e-beam exposure and then cross-linked by UV. Then 150 nm Au was deposited by thermal evaporation as the output electrode ( $V_{OUT}$ ) and patterned by photolithography.  $Subsequently, a \ p\text{-type} \ bg DPP\text{-}g2T \ blend \ solution \ was \ spin\text{-}coated \ at$ 3,000 r.p.m. for 20 s, patterned by e-beam exposure and cross-linked. A 150 nm Au film was deposited by thermal evaporation as the  $V_{\rm DD}$  and side-gate electrode and patterned by photolithography. Finally, the Au  $V_{\rm DD}$  and side-gate electrodes, the PEDOT:PSS film and the ion-gel were prepared as discussed above.

**Vertical NOR fabrication.** The Si/SiO $_2$  wafer substrate, the ground electrode and the n-type bHOMO-gDPP film were prepared as described above. Then 150 nm Au was deposited by thermal evaporation as the  $V_{\rm OUT}$  electrode and patterned by photolithography. The p-type bgDPP-g2T film was then prepared as discussed above. Then 150 nm Au was deposited by thermal evaporation as the node electrode and patterned by photolithography. Finally, the p-type bgDPP-g2T film, the Au  $V_{\rm DD}$  and side-gate electrodes, the PEDOT:PSS film and the ion-gel were prepared as discussed above.

**Organic semiconductor patterning.** All polymer semiconductors were patterned by e-beam exposure with a voltage of 50 kV, HC70 column mode with 18.683 nA beam current (Raith Voyager) and dose of  $300~\mu\text{C cm}^{-2}$ .

#### Device and film characterization

All OECTs, OECT arrays and circuits were characterized using an Agilent B1500A semiconductor parameter analyser in ambient air at room temperature. The EIS measurements were conducted using a PalmSens4 potentiostat (PalmSens). For the vertical EIS, OSCs were spin-coated onto  $600 \times 600 \,\mu m$  Au and patterned via sacrificial parylene peel. The materials were immersed in 0.1 M NaCl and an Ag/AgCl pellet electrode was used as a gate. Bias ranges of 0.5 V-0 V and -0.7 V-0 V were applied for the p- and n-types respectively. For the lateral configuration, reference and counter electrodes were connected to the drain electrode of an cOECT ( $W = 100 \, \mu \text{m}$ ,  $L = 10 \, \mu \text{m}$ ), and the source to the working electrode. The OSC was covered with 0.1 M NaCl, and 0 V d.c. with 10 mV alternating current (AC) oscillation was applied with frequency range from 1 to 10<sup>6</sup> Hz. For the cycling tests, the voltage pulse was generated by a Keysight waveform generator (33,600 A). For NAND and NOR characterization, square voltage pulses from 0 to ±0.7 V with a frequency of 5 Hz and 10 Hz were applied as  $V_{\text{IN-A}}$  and  $V_{\text{IN-B}}$ , respectively, by a Keysight waveform generator (33,600 A), and  $V_{OUT}$  was measured by an Agilent B1500A. SEM images were recorded with a Hitachi SU8030 FE-SEM. Film morphologies were characterized using cross-polarized optical microscopy (ECLIPSE LV150, Nikon) and AFM (Bruker ICON System). Two-dimensional GIWAXS measurements were performed at beamline 8-ID-E at the Advanced Photon Source at Argonne National Laboratory. The samples were irradiated at incidence angles from 0.130° to 0.140° in vacuum at 10.915 keV for two summed exposures of 2.5 s each. Signals were collected with a Pilatus 1 M detector located at a distance of 228.16 mm from the samples. FTIR spectra were obtained in the attenuated total reflectance (ATR) mode (Bruker LUMOS). UV-visible-near infrared spectra were measured with a Varian Cary 100 and Perkin Elmer LAMBDA 1050 UV-visible spectrophotometers. The XPS spectra were measured with a Thermo Scientific ESCALAB 250Xi instrument at a base pressure of  $2 \times 10^{-8}$  mbar.

# Data availability

Source data are provided with this paper. Additional data related to this work are available from the corresponding authors upon request.

#### References

- Chen, J. et al. Highly stretchable organic electrochemical transistors with strain-resistant performance. Nat. Mater. 21, 564–571 (2022).
- Andersson Ersman, P. et al. All-printed large-scale integrated circuits based on organic electrochemical transistors. Nat. Commun. 10, 5053 (2019).
- Park, S. et al. Self-powered ultra-flexible electronics via nano-gratingpatterned organic photovoltaics. Nature 561, 516–521 (2018).
- Stein, E. et al. Ambipolar blend-based organic electrochemical transistors and inverters. Nat. Commun. 13, 5548 (2022).
- Rashid, R. B. et al. Ambipolar inverters based on cofacial vertical organic electrochemical transistor pairs for biosignal amplification. Sci. Adv. 7, eabh1055 (2021).
- Picca, R. A. et al. Ultimately sensitive organic bioelectronic transistor sensors by materials and device structure design. Adv. Funct. Mater. 30, 1904513 (2020).
- Torricelli, F. et al. Electrolyte-gated transistors for enhanced performance bioelectronics. Nat. Rev. Meth. Primers 1, 66 (2021).
- 8. Abarkan, M. et al. Vertical organic electrochemical transistors and electronics for low amplitude micro-organ signals. *Adv. Sci.* **9**, 2105211 (2022).
- Spyropoulos, G. D., Gelinas, J. N. & Khodagholy, D. Internal ion-gated organic electrochemical transistor: a building block for integrated bioelectronics. Sci. Adv. 5, eaau7378 (2020).
- Harikesh, P. C. et al. Ion-tunable antiambipolarity in mixed ion-electron conducting polymers enables biorealistic organic electrochemical neurons. *Nat. Mater.* 22, 242–248 (2023).

- 11. Song, J. et al. 2D metal-organic frameworks for ultraflexible electrochemical transistors with high transconductance and fast response speeds. *Sci. Adv.* **9**, eadd9627 (2023).
- Wang, Y. et al. n-type organic electrochemical transistors with high transconductance and stability. Chem. Mater. 35, 405–415 (2023).
- 13. Rivnay, J. et al. Organic electrochemical transistors. *Nat. Rev. Mater.* **3**, 17086 (2018).
- 14. Wu, X. et al. High performing solid-state organic electrochemical transistors enabled by glycolated polythiophene and ion-gel electrolyte with a wide operation temperature range from –50 to 110°C. Adv. Funct. Mater. 33, 2209354 (2023).
- Cea, C. et al. Enhancement-mode ion-based transistor as a comprehensive interface and real-time processing unit for in vivo electrophysiology. *Nat. Mater.* 19, 679–686 (2020).
- Khodagholy, D. et al. High transconductance organic electrochemical transistors. Nat. Commun. 4, 2133 (2013).
- Schmatz, B., Lang, A. W. & Reynolds, J. R. Fully printed organic electrochemical transistors from green solvents. *Adv. Funct. Mater.* 29, 1905266 (2019).
- Jiang, C., De Rijk, S. R., Malliaras, G. G. & Bance, M. L. Electrochemical impedance spectroscopy of human cochleas for modeling cochlear implant electrical stimulus spread. *APL Mater.* 8, 091102 (2020).
- Koutsouras, D. A., Torricelli, F. & Blom, P. W. M. Submicron vertical channel organic electrochemical transistors with ultrahigh transconductance. Adv. Electron. Mater. 9, 2200868 (2023).
- Kleemann, H., Krechan, K., Fischer, A. & Leo, K. A review of vertical organic transistors. Adv. Funct. Mater. 30, 1907113 (2020).
- 21. Huang, W. et al. Vertical organic electrochemical transistors for complementary circuits. *Nature* **613**, 496–502 (2023).
- 22. Kim, J. et al. Scalable sub-micron patterning of organic materials toward high density soft electronics. *Sci. Rep.* **5**, 14520 (2015).
- Zheng, Y. Q. et al. Monolithic optical microlithography of high-density elastic circuits. Science 373, 88–94 (2021).
- 24. Wang, S. et al. Skin electronics from scalable fabrication of an intrinsically stretchable transistor array. *Nature* **555**, 83–88 (2018).
- Chortos, A. et al. Mechanically durable and highly stretchable transistors employing carbon nanotube semiconductor and electrodes. Adv. Mater. 28, 4441–4448 (2016).
- Malinowski, P. E. et al. Photolithographic patterning of organic photodetectors with a non-fluorinated photoresist system. Org. Electron. 15, 2355–2359 (2014).
- Chang, J. F., Gwinner, M. C., Caironi, M., Sakanoue, T. & Sirringhaus, H. Conjugated-polymer-based lateral heterostructures defined by high-resolution photolithography. Adv. Funct. Mater. 20, 2825–2832 (2010).
- Gangnaik, A. S., Georgiev, Y. M. & Holmes, J. D. New generation electron beam resists: a review. Chem. Mater. 29, 1898–1917 (2017).
- Qin, N. et al. Nanoscale probing of electron-regulated structural transitions in silk proteins by near-field IR imaging and nano-spectroscopy. *Nat. Commun.* 7, 13079 (2016).
- Blanksby, S. J. & Ellison, G. B. Bond dissociation energies of organic molecules. Acc. Chem. Res. 36, 255–263 (2003).
- 31. Bässler, H. & Köhler, A. Charge transport in organic semiconductors. *Top. Curr. Chem.* **312**, 1–65 (2012).
- 32. Liu, G. et al. Ultralow-power and multisensory artificial synapse based on electrolyte-gated vertical organic transistors. *Adv. Funct. Mater.* **32**, 2200959 (2022).
- 33. Lenz, J., del Giudice, F., Geisenhof, F. R., Winterer, F. & Weitz, R. T. Vertical, electrolyte-gated organic transistors show continuous operation in the MA cm<sup>-2</sup> regime and artificial synaptic behaviour. *Nat. Nanotechnol.* **14**, 579–585 (2019).
- 34. Xie, Z. et al. All-solid-state vertical three-terminal N-type organic synaptic devices for neuromorphic computing. *Adv. Funct. Mater.* **32**, 2107314 (2022).

- Guo, E. et al. Vertical organic permeable dual-base transistors for logic circuits. Nat. Commun. 11, 4725 (2020).
- 36. Huggins, R. A. Simple method to determine electronic conductivity and ionic components of the conductors in mixed a review. *Ionics* **8**, 300–313 (2002).
- Wang, Y. et al. Hybrid alkyl-ethylene glycol side chains enhance substrate adhesion and operational stability in accumulation mode organic electrochemical transistors. *Chem. Mater.* 31, 9797–9806 (2019).
- Wu, H. Y. et al. Influence of molecular weight on the organic electrochemical transistor performance of ladder-type conjugated polymers. Adv. Mater. 34, 2106235 (2022).
- 39. Ohayon, D. et al. Influence of side chains on the n-type organic electrochemical transistor performance. ACS Appl. Mater. Interfaces 13, 4253–4266 (2021).
- 40. Giovannitti, A. et al. N-type organic electrochemical transistors with stability in water. *Nat. Commun.* **7**, 13066 (2016).
- 41. Yan, Y. et al. High-performance organic electrochemical transistors with nanoscale channel length and their application to artificial synapse. ACS Appl. Mater. Interfaces 12, 49915–49925 (2020).
- Savva, A. et al. Solvent engineering for high-performance n-type organic electrochemical transistors. Adv. Electron. Mater. 5, 1900249 (2019).
- Wu, X. et al. Universal spray-deposition process for scalable, high-performance, and stable organic electrochemical transistors. ACS Appl. Mater. Interfaces 12, 20757–20764 (2020).
- 44. Moser, M. et al. Side chain redistribution as a strategy to boost organic electrochemical transistor performance and stability. *Adv. Mater.* **32**, 2002748 (2020).
- Chércoles Asensio, R., San Andrés Moya, M., De La Roja, J. M. & Gómez, M. Analytical characterization of polymers used in conservation and restoration by ATR-FTIR spectroscopy. *Anal. Bioanal. Chem.* 395, 2081–2096 (2009).
- Kim, J. et al. Vertically stacked full color quantum dots phototransistor arrays for high-resolution and enhanced color-selective imaging. Adv. Mater. 34, 2106215 (2022).
- 47. Lee, W. et al. Transparent, conformable, active multielectrode array using organic electrochemical transistors. *Proc. Natl Acad. Sci. USA* **114**, 10554–10559 (2017).
- Lee, W. et al. Nonthrombogenic, stretchable, active multielectrode array for electroanatomical mapping. Sci. Adv. 4, eaau2426 (2018).
- 49. Weissbach, A. et al. Photopatternable solid electrolyte for integrable organic electrochemical transistors: Operation and hysteresis. *J. Mater. Chem. C.* **10**, 2656–2662 (2022).
- Kang, J. et al. Symmetrically ion-gated in-plane metal-oxide transistors for highly sensitive and low-voltage driven bioelectronics. Adv. Sci. 9, 2103275 (2022).
- Koutsouras, D. A., Torricelli, F., Gkoupidenis, P. & Blom, P. W.
  M. Efficient gating of organic electrochemical transistors with in-plane gate electrodes. Adv. Mater. Technol. 6, 2100732 (2021).
- 52. Rivnay, J. et al. Organic electrochemical transistors with maximum transconductance at zero gate bias. *Adv. Mater.* **25**, 7010–7014 (2013).
- Song, C. K., Eckstein, B. J., Tam, T. L. D., Trahey, L. & Marks, T. J. Conjugated polymer energy level shifts in lithium-ion battery electrolytes. ACS Appl. Mater. Interfaces 6, 19347–19354 (2014).
- Wang, Z. et al. Cinnamate-functionalized natural carbohydrates as photopatternable gate dielectrics for organic transistors. Chem. Mater. 31, 7608–7617 (2019).
- Kostianovskii, V., Sanyoto, B. & Noh, Y. Y. A facile way to pattern PEDOT:PSS film as an electrode for organic devices. *Org. Electron.* 44, 99–105 (2017).

# **Acknowledgements**

This work was supported by the AFOSR (contract no. FA9550-22-1-0423), the US Office of Naval Research Contract no. N00014-20-1-2116, by the US Department of Commerce, National Institute of Standards and Technology as part of the Centre for Hierarchical Materials Design Award no. 70NANB10H005, BSF (award no. 2020384), NSF (DMR-2223922) and the Northwestern University Materials Research Science and Engineering Center Awards NSF DMR-1720139 and DMR-2308691. J.R. gratefully acknowledges support from the Alfred P. Sloan Foundation (FG-2019-12046). This work acknowledges the US Department of Energy under contract no. DE-ACO2-05CH11231 at beamline 8-ID-E of the Advanced Photon Source, a US Department of Energy (DOE) Office of Science User Facility operated for the DOE Office of Science by Argonne National Laboratory under Contract No. DE-ACO2-06CH11357. This work made use of the NUFAB facility of Northwestern University's NUANCE Center, which has received support from the SHyNE Resource (NSF ECCS-2025633), the IIN and Northwestern's MRSEC programme (NSF DMR-1720139).

### **Author contributions**

J.K., T.J.M. and A.F. conceived and designed the research. J.K. carried out the device fabrication, characterizations and demonstrations. R.M.P. and Y.C. synthesized the polymer semiconductors. J.K., R.M.P., I.D.D., F.Q., D.Z. and W.H. analysed the data. D.M., R.D. and J.R. conducted the bandwidth and EIS measurements. R.M.P. and I.D.D. measured and analysed the GIWAXS. All the authors discussed the results and commented on the manuscript. J.K., J.R., T.J.M. and A.F. wrote the manuscript.

# **Competing interests**

A patent application has been filed by Northwestern with inventors J.K., T.J.M. and A.F. The remaining authors declare no competing interests.

#### **Additional information**

**Supplementary information** The online version contains supplementary material available at https://doi.org/10.1038/s41928-024-01127-x.

**Correspondence and requests for materials** should be addressed to Jonathan Rivnay, Tobin J. Marks or Antonio Facchetti.

**Peer review information** *Nature Electronics* thanks Wei Lin Leong and the other, anonymous, reviewer(s) for their contribution to the peer review of this work.

**Reprints and permissions information** is available at www.nature.com/reprints.

**Publisher's note** Springer Nature remains neutral with regard to jurisdictional claims in published maps and institutional affiliations.

Springer Nature or its licensor (e.g. a society or other partner) holds exclusive rights to this article under a publishing agreement with the author(s) or other rightsholder(s); author self-archiving of the accepted manuscript version of this article is solely governed by the terms of such publishing agreement and applicable law.

© The Author(s), under exclusive licence to Springer Nature Limited 2024